

# IterMask3D: Unsupervised Anomaly Detection and Segmentation with Test-Time Iterative Mask Refinement in 3D Brain MRI

Ziyun Liang<sup>a</sup>, Xiaoqing Guo<sup>a,b</sup>, Wentian Xu<sup>a</sup>, Yasin Ibrahim<sup>a</sup>, Natalie Voets<sup>c</sup>, Pieter M Pretorius<sup>d</sup>, J. Alison Noble<sup>a</sup> and Konstantinos Kamnitsas<sup>a</sup>

<sup>a</sup>*Department of Engineering Science, University of Oxford, UK*

<sup>b</sup>*Department of Computer Science, Hong Kong Baptist University*

<sup>c</sup>*Nuffield Department of Clinical Neurosciences, University of Oxford*

<sup>d</sup>*Department of Neuroradiology, Oxford University Hospitals NHS Foundation Trust*

## ARTICLE INFO

### Keywords:

Unsupervised Anomaly Segmentation  
3D Brain MRI  
Anomaly Detection

## ABSTRACT

Unsupervised anomaly detection and segmentation methods train a model to learn the training distribution as ‘normal’. In the testing phase, they identify patterns that deviate from this normal distribution as ‘anomalies’. To learn the ‘normal’ distribution, prevailing methods corrupt the images and train a model to reconstruct them. During testing, the model attempts to reconstruct corrupted inputs based on the learned ‘normal’ distribution. Deviations from this distribution lead to high reconstruction errors, which indicate potential anomalies. However, corrupting an input image inevitably causes information loss even in normal regions, leading to suboptimal reconstruction and an increased risk of false positives. To alleviate this, we propose IterMask3D, an iterative spatial mask-refining strategy designed for 3D brain MRI. We iteratively spatially mask areas of the image as corruption and reconstruct them, then shrink the mask based on reconstruction error. This process iteratively unmasks ‘normal’ areas to the model, whose information further guides reconstruction of ‘normal’ patterns under the mask to be reconstructed accurately, reducing false positives. In addition, to achieve better reconstruction performance, we also propose using high-frequency image content as additional structural information to guide the reconstruction of the masked area. Extensive experiments on the detection of both synthetic and real-world imaging artifacts, as well as segmentation of various pathological lesions across multiple MRI sequences, consistently demonstrate the effectiveness of our proposed method. Code is available at <https://github.com/ZiyunLiang/IterMask3D>.

## 1. Introduction

Segmenting anomalies is crucial in the field of medical image analysis as it enables applications such as early disease detection and diagnosis, guides treatment planning, and reduces clinical workload. Conventional anomaly segmentation methods are mostly supervised, relying on annotated training data, where images contain anomalies with corresponding manual labels. Trained on a limited set of data types, the model can only segment anomalies resembling those in its training data, and struggles to detect other types of unseen anomalies. In the context of brain MRI images, the focus of this study, this type of methods typically target a specific pathology (Kamnitsas, Ledig, Newcombe, Simpson, Kane, Menon, Rueckert and Glocker, 2017; Isensee, Jäger, Full, Vollmuth and Maier-Hein, 2021; Stollenga, Byeon, Liwicki and Schmidhuber, 2015). Unsupervised anomaly segmentation, on the other hand, does not require any ‘anomalous’ images or their manual segmentations during training. Instead, it is trained exclusively on ‘normal’ images and treats this training distribution as the ‘normal’ reference. During testing, the method regards any deviation from this reference as ‘anomaly’ and attempts to segment it. This enables the detection of previously unseen patterns, including new pathologies or even imaging artifacts, making it

suitable for tasks such as automatic screening for incidental findings (Rowley, Paukner, Eisenmenger, Field, Davidson, Johnson, Asthana, Chin, Prabhakaran, Bendlin et al., 2023) or automatic scan quality control (Hendriks, Mutsaerts, Joules, Peña-Nogales, Rodrigues, Wolz, Burchell, Barkhof and Schranter, 2024). Such an approach is especially beneficial when training data are limited and the specific pathology type is unknown in advance, facilitating the detection of rare diseases. In this work, we explore unsupervised anomaly segmentation, with a focus on brain MRI data.

A prevalent strategy for learning the training distribution is reconstruction-based methods that follow the ‘corrupt and reconstruct’ paradigm. During training, images are first artificially corrupted, then models are trained to reconstruct the provided ‘normal’ in-distribution images, thus internalizing the normal distribution through the reconstruction process. At testing, regions that deviate from the learned normal distribution, i.e., anomalies, tend to yield high reconstruction errors, which can then be exploited for segmentation. Common ways of adding corruptions include compression (Atlason, Love, Sigurdsson, Gudnason and Ellingsen, 2019; Baid, Ghodasara, Mohan, Bilello, Calabrese, Colak, Farahani, Kalpathy-Cramer, Kitamura, Pati et al., 2021) or noise as in diffusion models (Pinaya, Graham, Gray, Da Costa, Tudosiu, Wright, Mah, MacKinnon, Teo, Jager et al., 2022a; Bercea, Neumayr, Rueckert and Schnabel, 2023a; Wolleb, Bieder, Sandkühler and Cattin, 2022), where the model is

\*Corresponding author.

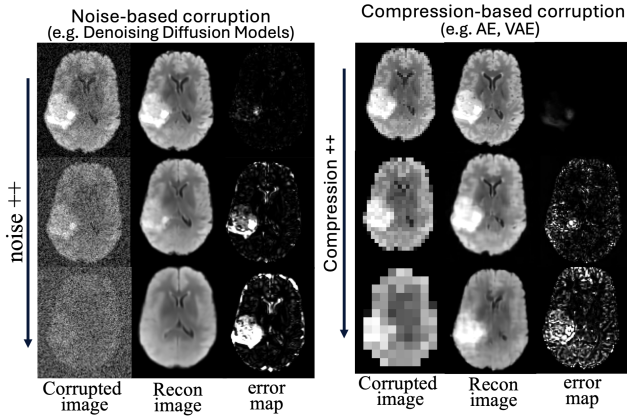


**Figure 1: Sensitivity–Precision Trade-off** in reconstruction-based methods: When corruption (e.g., noise or compression) is lower, the reconstruction error over anomalous regions (the hyper-intense tumor) remains low, often resulting in missed detections. As corruption increases, errors in abnormal regions become more pronounced, improving sensitivity—but at the cost of higher errors in normal regions, which can increase false positives and reduce precision.

tasked to reconstruct from these corruptions. A common challenge of these types of methods is *sensitivity-precision trade-off*, as shown in Fig. 1. In order to amplify reconstruction error in abnormal areas for better segmentation, more corruption is preferred. However, since the location of anomalies is unknown in advance, corruption is applied to the entire image. Thus, more corruptions will not only increase the reconstruction error in abnormal area, but it will also increase it in normal areas, which leads to false positives. As shown in Fig. 1, increasing the noise level and compression results in higher reconstruction error over the anomaly (in this case, the hyper-intense tumor), thus leads to better detection of the anomaly area. But at the same time, normal areas also have larger reconstruction errors, leading to false positives. This *sensitivity-precision trade-off* serves as the main motivation of our paper: *Can we use input corruptions to amplify reconstruction errors in anomalous areas for better segmentation, while preserving the information in normal areas to minimize reconstruction errors and reduce false positives?*

To address this problem, we propose *IterMask3D*, an iterative mask refinement method for unsupervised anomaly segmentation and detection that can be used on 3D MRI data. To amplify reconstruction errors in anomalous regions, we introduce spatial masking as a form of corruption. To minimize errors in normal regions, we employ an iterative spatial mask shrinking process, gradually refining the mask toward the anomaly to reduce information loss. As normal tissues are progressively unmasked and fed into the model, they guide the reconstruction of normal structures beneath the mask to reduce false positives. Additionally, we generate a structural image using high-frequency masking, providing

structural guidance to steer the reconstruction of normal areas for the mask-shrinking process.

Our main contributions are:

(1) We propose a 3D unsupervised anomaly segmentation and detection method *IterMask3D*, which iteratively shrinks a spatial mask towards the anomaly to reduce false positives on normal areas.

(2) We further propose the use of frequency masking to generate high-frequency images as structural guidance for the mask-shrinking process, enhancing the reconstruction of normal areas and further reducing false positives.

(3) We introduce a subject-specific thresholding strategy that determines, at each iteration, which regions on the error map can be confidently classified as normal. This allows the iterative mask-shrinking process to automatically determine the optimal stopping point for each individual subject without the need to require extra information from validation data.

(4) We evaluate the effectiveness of our method on diverse types of anomalies, including both pathological and artifact-based abnormalities. Specifically, we test our model on synthetic and real-world artifacts, as well on tumor and stroke as pathologies across multiple MRI sequences.

This paper builds upon our previous work (Liang, Guo, Noble and Kamnitsas, 2024), where we introduced Iterative Mask Refinement (*IterMask<sup>2</sup>*) for unsupervised anomaly segmentation in 2D brain MRI pathology. The 2D-based model follows the standard practice of anomaly segmentation, where it is trained on healthy slices and evaluated on anomaly slices from the same dataset. This builds upon it by: (a) extending the method to 3D and evaluate it on real-world training and testing data from different distributions, further advancing its applicability to real-world settings. (b) We extend our evaluation beyond pathological anomalies to include imaging artifacts, assessing the model’s effectiveness in detecting both types of anomalies. (c) Instead of relying on a fixed threshold for the entire dataset, we adopt an image-specific thresholding strategy that automatically determines when to stop the mask-shrinking process—without requiring access to any validation data. (d) In the last work, our method required two separate models: one for the initial prediction when masking the whole brain area and another for the subsequent mask-shrinking process. In this work, we unify these steps into a single model for the entire mask-shrinking process. (e) We extend the mask refinement process to support both shrinking and expansion, allowing more flexible and being able to correct the mistakes from previous steps.

The rest of the paper is organized as follows. The related works are described in Section 2. Our method *IterMask3D* is introduced in Section 3 where an overview of the method is provided in Subsection 3.1. We describe iterative spatial mask refinement in Subsection 3.2, frequency masking in Subsection 3.3, threshold selecting strategy in Subsection 3.4, and the overall training process in Subsection 3.5 in detail. Finally, the experimental results are presented in Section 4, covering four tasks: detection of synthetic artifacts (Subsection 4.2), detection of real-world artifacts

(Subsection 4.3), pathology segmentation on 2D data (Subsection 4.4), and pathology segmentation on 3D data (Subsection 4.5).

## 2. Related Work

**Reconstruction-based unsupervised anomaly segmentation:** These approaches are among the most prevalent for unsupervised anomaly segmentation, typically following a ‘corrupt and reconstruct’ paradigm (as outlined in Section 1). The core idea is to learn the distribution of normal data by training a model to reconstruct inputs after they have been deliberately corrupted. One way to achieve this corruption is via compression, as used by Autoencoders (AE) (Atlason et al., 2019; Baur, Denner, Wiestler, Navab and Albarqouni, 2021; Cai, Chen and Cheng, 2024), Variational Autoencoders (VAE) (Baur et al., 2021; Pawlowski, Lee, Rajchl, McDonagh, Ferrante, Kamnitsas, Cooke, Stevenson, Khetani, Newman et al., 2018; Zimmerer, Isensee, Petersen, Kohl and Maier-Hein, 2019), and Vector Quantized Variational Autoencoders (VQ-VAE) (Pinaya, Tudosiu, Gray, Rees, Nachev, Ourselin and Cardoso, 2022b). Another common strategy, generative models, employs noise as corruption. Among these methods, f-AnoGAN (Schlegl, Seeböck, Waldstein, Langs and Schmidt-Erfurth, 2019) builds on Generative Adversarial Networks (GANs), but the notoriously unstable training of GANs often limits their practical applicability. Recently, diffusion models (Ho, Jain and Abbeel, 2020) have shown promise across diverse medical imaging tasks (Wu, Fu, Fang, Zhang, Yang, Xiong, Liu and Xu, 2024; Khader, Müller-Franzes, Tayebi Arasteh, Han, Haarbuerger, Schulze-Hagen, Schad, Engelhardt, Baeßler, Foersch et al., 2023; Zheng, Mo, Sun, Li, Wu, Wang, Vincent and Papież, 2024), with applications extending to unsupervised anomaly segmentation (Bercea et al., 2023a; Wolleb et al., 2022; Pinaya et al., 2022a). In these approaches, inputs are typically corrupted with a certain level of Gaussian noise (Pinaya et al., 2022a; Bercea et al., 2023a) before being reconstructed.

A key challenge in reconstruction-based methods is determining how much corruption (e.g. compression or noise) to inject. While greater corruption can amplify reconstruction errors in anomalous regions, it inevitably degrades normal areas as well, increasing false positives (Bercea, Rueckert and Schnabel, 2023b). We refer to this balance between capturing anomalies (sensitivity) and preserving normal regions (precision) as the *sensitivity-precision trade-off* (Fig. 1). One of our primary objectives is to alleviate this trade-off by ensuring that reconstruction errors remain high for anomalies while staying low for normal areas.

Several efforts have been made in this direction; for instance, (Bercea et al., 2023a) proposes an iterative process where a mask covering all anomalies is generated first, and then the masked region is reconstructed using a diffusion model. Although similar in its iterative design, this approach does not refine the potentially suboptimal initial mask, nor does it leverage auxiliary guidance to accurately reconstruct

the masked content. As a result, it can struggle to faithfully recover normal tissues. Our method overcomes these issues more effectively, as we will demonstrate.

**Non-reconstruction-based unsupervised anomaly segmentation:** A transformer-based approach is introduced in (Pinaya et al., 2022b), where a VQ-VAE serves as the foundational architecture. The method enhances the standard reconstruction-based framework by incorporating a transformer as an autoregressive model operating on the compressed latent representations. This work was applied to 3D brain MRI for anomaly detection, using only ‘healthy’ subjects for training as normal and subsequently identifying pathologies as anomalies. However, the transformer component requires an ensemble prediction of differently-ordered latent representations, leading to inefficient computation.

Recently, cross-sequence translation has been proposed for reconstruction (Liang, Anthony, Wagner and Kamnitsas, 2023). In this approach, a model is trained to translate normal tissues between different MRI sequences, with the assumption that anomalies will fail to be translated correctly and can thus be segmented. However, this method requires multi-modal data and may suffer from information loss if features are not fully shared across sequences, potentially leading to false positives.

Another type of method that shows promising performance is the denoising-based methods (Kascenas, Pugeault and O’Neil, 2022). Unlike ‘corrupt and reconstruct’, this adds noise to inputs only during *training* (not testing), then learns to remove it. During testing, anomalies are treated as noise and removed. A key limitation, however, is that the noise added during training must approximate the appearance of anomalies, requiring prior knowledge of their morphology. This constraint is impractical when aiming to detect all pathologies, as we do in this work.

## 3. Methods

### 3.1. The overview

Our proposed method is a reconstruction-based unsupervised anomaly segmentation method. The training dataset,  $D_{tr} = \{\mathbf{x}^i\}_{i=1}^N$ , consists of ‘normal’ in-distribution samples. The model aims to learn the training distribution following the ‘corrupt and reconstruct’ paradigm as previously introduced in Section 1, which learns to reconstruct in-distribution samples after corruption. During testing, given testing dataset  $D_{te} = \{\mathbf{x}^i\}_{i=1}^M$ , the model aims to segment any patterns outside the training distribution (unseen during training) as anomalies. To mitigate the sensitivity-precision trade-off in reconstruction-based methods, we propose an iterative spatial mask refinement process, *IterMask3D* as shown in Fig. 2 (c) *Testing Process*. To ensure large reconstruction errors in abnormal regions for effective anomaly segmentation, spatial masking is applied to completely mask anomalies before reconstruction. Additionally, to accurately reconstruct normal areas with minimal reconstruction error, we gradually shrink the mask towards the anomaly. This process progressively unmask normal regions, providing

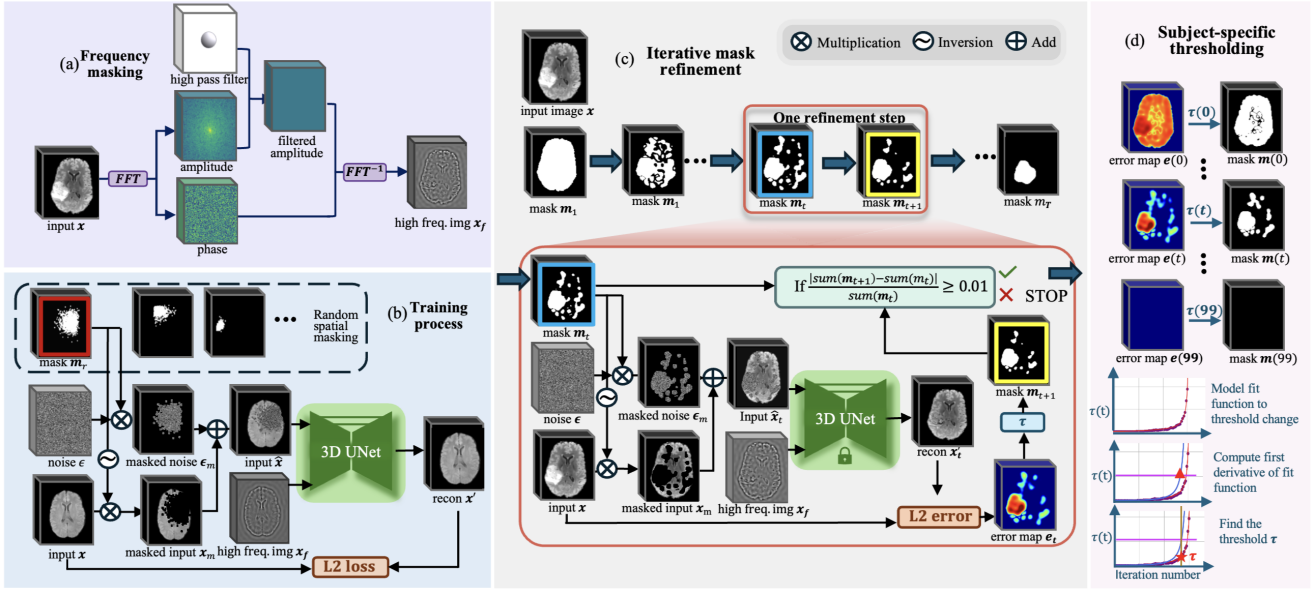


**Figure 2: Overview of the proposed approach.** (a) Frequency-based masking: Extract structural information  $x_f$  with a high-pass filter to isolate the high-frequency components of the image. (b) Training process: Input image  $x$  is masked using random spatial masking, and the model learns to reconstruct the masked area with  $x_f$  generated in (a) as an auxiliary input. (c) Iterative mask refinement: Iterative refinement of the spatial mask, where the mask  $m_t$  at iteration  $t$  gradually shrinks towards the anomalous region. This refinement is guided by the spatially unmasked portions of the image  $x_m$  and  $x_f$  from (a). (d) Subject-Specific Thresholding: This component illustrates how the threshold  $\tau$  is determined for iterative mask refinement on a per-sample basis. The mask is progressively shrunk by 1% of the brain volume at each time step  $t$  until it fully disappears. We model  $\tau(t)$  using a fitted function, and compute its derivative to identify the point where the threshold begins to change abruptly. This point is selected as the sample-specific threshold  $\tau$  for the current sample.

the network with more information on case-specific ‘normal’ patterns to better reconstruct normal areas under the mask.

Specifically, as shown in Fig. 2 (c) *Iterative mask Process*, we start by masking the entire brain area. In each iteration, the network reconstructs the masked regions and areas with small errors are identified as normal and subsequently unmasked. With every iteration, more information is revealed, allowing the network to refine its reconstruction.

The threshold for identifying normal regions in each iteration is decided by the *Subject-specific thresholding* strategy, as shown in Fig. 2 (d). As the mask is progressively shrunk by a fixed proportion, the threshold is selected based on the characteristic change in threshold values throughout the mask-shrinking process.

However, as the network is guided only by the unmasked regions, it must infer the missing structures in a generative manner. Incorrectly inferred structures will introduce reconstruction errors even in normal areas, leading to false positives. To address this, we further propose incorporating high-frequency information (achieved via low-frequency masking in the Fourier space) to guide the structural reconstruction of masked regions, as shown in Fig. 2 (a).

Finally, the training process is depicted in Fig. 2 (b). To train the reconstruction model, we apply randomly generated Gaussian masks as spatial masks to the input image and combine them with input of high-frequency components (generated as shown in Fig.2(a)). The model is trained to

reconstruct the masked regions using this combined input. In the following sections, we introduce Iterative Spatial Mask Refinement (Fig.2 (c)) in Section 3.2, frequency masking (Fig.2 (a)) in Section 3.3, subject-specific thresholding strategy (Fig.2 (d)) in Section 3.4, and the training process (Fig.2 (b)) in Section 3.5.

### 3.2. Iterative Spatial Mask Refinement for Testing

In this section, we provide a detailed explanation of how our iterative spatial mask refinement method works during testing. The process iteratively refines the spatial mask towards the anomaly as shown in the top part of Fig. 2 (c). We define the iteration number as  $t$ , where  $t = 0, 1, \dots, T$ . In the first iteration ( $t = 0$ ), given an input test image  $\mathbf{x}$ , the spatial mask starts shrinking from an initial mask covering the entire brain  $\mathbf{m}_0$ . The mask is then progressively shrunk to mask  $\mathbf{m}_t$  at iteration  $t$ , narrowing its focus towards the anomaly, until the final mask reaches  $\mathbf{m}_T$ .

To describe the process in greater detail, we focus on one iteration  $t$  extracted from the complete mask shrinking process as shown in the bottom part of Fig. 2 (c). The input to this iteration is original test image  $\mathbf{x}$  and mask  $\mathbf{m}_t$ . Gaussian noise  $\epsilon$  is generated with the same dimensions as the original test image, and it is used to cover the masked area in the image  $\epsilon_m$  (Eq. 1). The unmasked area is already confidently identified as normal from previous iterations so copied directly from the input image  $\mathbf{x}_m$  (Eq. 2). Then they

are added together as the input to the model at iteration  $t$  as  $\hat{\mathbf{x}}_t$  (Eq. 3):

$$\epsilon_m = \mathbf{m}_t \odot \epsilon \quad (1)$$

$$\mathbf{x}_m = \mathbf{x} \odot (1 - \mathbf{m}_t) \quad (2)$$

$$\hat{\mathbf{x}}_t = \epsilon_m + \mathbf{x}_m \quad (3)$$

Here,  $\odot$  represents element-wise multiplication. Then, the masked image  $\hat{\mathbf{x}}_t$  and high frequency image  $\mathbf{x}_f$  is input to our model  $f$  to reconstruct the spatially masked areas. The model outputs reconstructed prediction  $\mathbf{x}'_t$ :

$$\mathbf{x}'_t = f(\hat{\mathbf{x}}_t, \mathbf{x}_f) \quad (4)$$

The high-frequency image  $\mathbf{x}_f$  here is an additional condition to the model, which will be discussed in Section 3.3. After the model reconstructs the masked area, we compute the  $L_2$  distance as an error map between the reconstructed image  $\mathbf{x}'_t$  and the original test image  $\mathbf{x}$ :

$$\mathbf{e}_t = \|\mathbf{x}'_t - \mathbf{x}\|_2 \quad (5)$$

Then, on the error map, we decide where is confidently identified as normal in the current iteration by comparing the error map  $\mathbf{e}_t$  with a threshold  $\tau_{stop}$ . Pixels with error that are below the specified threshold,  $\tau_{stop}$ , will be removed from the masked area, and the mask will shrink accordingly (Eq. 6). A detailed analysis on selecting the optimal  $\tau_{stop}$  for current sample can be found in Section 3.4.

$$\mathbf{m}_{t+1}(i, j) = \begin{cases} 0, & \text{if } \mathbf{e}_t(i, j) < \tau_{stop} \\ 1, & \text{otherwise} \end{cases} \quad (6)$$

When most of the spatially masked areas are anomalies, introducing more information will not reduce the high error in the anomalous areas and the mask will stop shrinking (shrink less than 1%), which is how we terminate the testing process.

### 3.3. Frequency Masking

In frequency domain analysis, an image is decomposed into its constituent spatial frequencies using transformations such as the Fourier Transform. Low-frequency components correspond to smooth intensity variations and capture intensities of large-scale image features, including the mean image intensity (DC signal). High-frequency components, on the other hand, encode rapid intensity changes, representing fine-grained details such as edges, textures, tissue boundaries, and the fine-grained contours of anatomical structures (Chappell, 2019). As part of frequency decomposition, an image can also be characterized by its amplitude and phase components. While the amplitude spectrum determines how strongly each frequency contributes to the overall image, the phase spectrum preserves spatial relationships, ensuring that structures and textures are correctly positioned (Oppenheim and Lim, 1981; Oppenheim, Lim, Kopec and Pohlig, 1979).

In our model  $f$  from the last section, spatial mask reconstruction relies solely on the unmasked area. However, due

---

#### noend 1 Iterative Spatial Mask Refinement (IterMask3D)

---

**Require:** 3D Brain MRI ( $\mathbf{x} \in D_{te}$ ), High-Frequency Image ( $\mathbf{x}_f$ ), Subject-specific Threshold ( $\tau_{stop}$ ) (Section 3.4)

**Ensure:** Anomaly Mask ( $\mathbf{m}_T$ )

1:  $\mathbf{m}_0 = \mathbf{1}, \quad t = 0$

2: **while** mask is still shrinking i.e.  $\frac{|\sum(\mathbf{m}_{t+1}) - \sum(\mathbf{m}_t)|}{\sum(\mathbf{m}_t)} < 0.01$

**do**

3:  $\epsilon \sim \mathcal{N}(0, 1)$

▷ Add noise to the masked area

4:  $\epsilon_m = \mathbf{m}_t \odot \epsilon$

▷ Leave the unmasked area unchanged

5:  $\mathbf{x}_m = \mathbf{x} \odot (1 - \mathbf{m}_t)$

▷ Combine these two to obtain a new image

6:  $\hat{\mathbf{x}} = \epsilon_m + \mathbf{x}_m$

▷ Predict based on combined and high-frequency image

7:  $\mathbf{x}'_t = f(\hat{\mathbf{x}}, \mathbf{x}_f)$

▷ Obtain  $L_2$  distance error map for masked area

8:  $\mathbf{e}_t = \|\mathbf{x}'_t - \mathbf{x}\|_2$

▷ For each pixel, unmask areas with error smaller than  $\tau_{stop}$

9:  $\mathbf{m}_{t+1}(i, j) = \begin{cases} 0, & \text{if } \mathbf{e}_t(i, j) < \tau_{stop} \\ 1, & \text{otherwise} \end{cases}$

10:  $t = t + 1$

11: **return**  $\mathbf{m}_T$

---

to the variability in human tissue structure, the model may generate a plausible yet structurally different reconstruction from the actual brain, leading to reconstruction errors even in normal regions. To address this, we introduce a high-frequency image as a conditioning input, providing structural guidance to the model. Since the model has not been trained to reconstruct anomalies from their high-frequency components, this approach reduces reconstruction errors in normal areas while preserving high reconstruction errors in anomalous regions.

To be more specific, when generating high-frequency images, we first apply Discrete Fourier Transform (DFT), denoted as  $\mathcal{F}$ , to map the input  $\mathbf{x}$  into the frequency domain, obtaining its frequency representation. The input image  $\mathbf{x}$  has dimensions  $H \times W$  and a spatial pixel value  $\mathbf{x}(h, w)$  at position  $(h, w)$ . The Fourier transform is defined as follows.

$$\mathcal{F}(\mathbf{x})(a, b) = \sum_{h=0}^{H-1} \sum_{w=0}^{W-1} e^{-i2\pi\left(\frac{ah}{H} + \frac{bw}{W}\right)} \mathbf{x}(h, w) \quad (7)$$

where the output  $\mathcal{F}(\mathbf{x})(a, b)$  is a complex-valued frequency representation, and  $(a, b)$  are spatial frequency indices representing each frequency component of the transformed image. In this complex frequency representation, let  $Im$  and  $Re$  denote the imaginary and real parts, respectively. The amplitude and phase of the frequency components can be

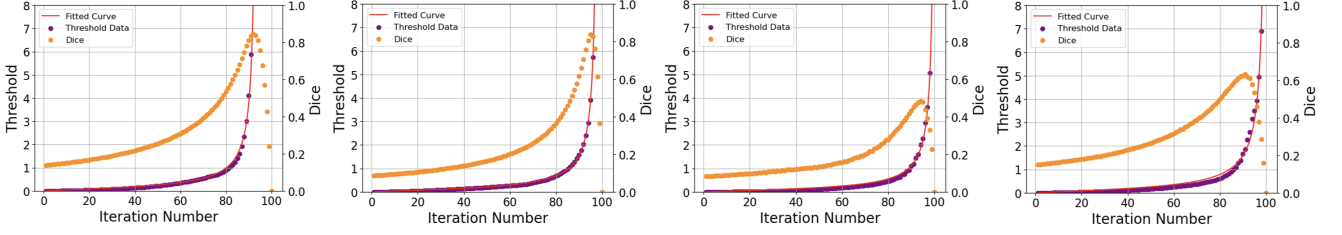


**Figure 3: Illustration of threshold dynamics with fixed shrinking speed of the mask.** The figures shown are plotted from four randomly chosen samples, two from the BraTS FLAIR sequence (left) and two from the BraTS T2 sequence (right). For each sample, the mask is progressively shrunk by 1% of the brain volume per iteration until it fully disappears. The purple points represent the threshold required to produce the current shrunken mask based on the reconstruction error map, with the red curve showing the fitted function. Orange points indicate the corresponding Dice scores between the mask and the ground truth anomaly at each iteration. As the mask approaches the anomaly, the Dice score increases and peaks when the anomaly is optimally exposed. Correspondingly, the corresponding threshold rises gradually, then sharply increases near the anomaly boundary—indicating a distinct shift in reconstruction error and serving as a marker for finding the optimal stopping threshold.

expressed as:

$$\mathcal{A} = |\mathcal{F}(\mathbf{x})(a, b)| \quad (8)$$

$$\phi = \tan^{-1} \frac{\text{Im}(\mathcal{F}(\mathbf{x})(a, b))}{\text{Re}(\mathcal{F}(\mathbf{x})(a, b))} \quad (9)$$

Next, to extract high-level structural information from the image, we focus on capturing the high-frequency components, which represent rapid intensity variations such as sharp edges and fine details. To achieve this, we apply a high-frequency filter that removes low-frequency amplitude components. Since the phase spectrum encodes the spatial structure of the image, we preserve the complete phase information to retain structural integrity. Therefore, our high-frequency filter for amplitude masking is:

$$N(u, v) = \begin{cases} 1, & \text{if } d((c_u, c_v), (u, v)) > r \\ 0, & \text{else} \end{cases}, \quad \mathcal{A}_m = \mathcal{A} \odot N \quad (10)$$

After obtaining the masked amplitude  $\mathcal{A}_m$  and retaining all phase information  $\phi$ , we apply the inverse Fourier transform, denoted as  $\mathcal{F}^{-1}$ , to the frequency domain representation  $\mathbf{x}_f$ . This transformation reconstructs the image back to the spatial domain, as shown below:

$$\mathbf{x}_f = \mathcal{A}_m * e^{j*\phi} \quad (11)$$

$$\mathbf{x} = \mathcal{F}^{-1}(\mathbf{x}_f) \quad (12)$$

### 3.4. Subject-Specific Thresholding Strategy

In this section, we discuss in detail the threshold strategy used to identify, for each image, in each iteration, which regions of the error map can be confidently identified as normal.

The original 2D approach in our previous work (Liang et al., 2024) applies a single fixed threshold  $\tau$  across all images within one sequence, and the threshold is selected using a validation set’s error map, under the assumption

that it reflects the model’s reconstruction error on unseen normal tissue. Thus, any error exceeding this threshold is then considered indicative of an anomaly. However, we identified two limitations that come with this approach when extending it to 3D MRI:

(1) For 3D datasets, it is usually impractical to acquire in-distribution validation data from the same clinical center with no distribution shift.

(2) One single threshold per dataset might not be optimal for each individual subject, as normal tissues can exhibit subject-specific intensity distributions and characteristics.

To address these limitations, we develop a per-image iteration-stopping strategy that does not rely on a threshold derived from external healthy validation data. This enables adaptive and subject-specific anomaly detection without requiring prior knowledge of the underlying distribution of normal tissue. For each image, we observe a distinct pattern about the value of reconstruction error at which we need to apply a threshold to shrink the mask by a given percent at each iteration of our process. A gradual and smooth increase of the threshold is required to progressively shrink the mask by a small percent over normal tissue between consecutive iterations. However, once the shrinking mask reaches the anomalous region, the threshold required to shrink the mask by a small percent rises abruptly. This sharp change reflects the significant reconstruction error triggered by the anomaly, highlighting a clear distinction between normal and abnormal tissue.

We extend our method to quantify and leverage this property for testing. During the iterative testing process, at each iteration  $t$  we apply a threshold  $\tau(t)$  to the reconstruction error mask such that the mask is shrunk by 1% of the brain volume per iteration, until the mask fully disappears. We show this process in Fig. 3. As the shrinking mask approaches the anomaly, which is shown with the Dice score with yellow dots in Fig. 3, the reconstruction error increases sharply, resulting in an abrupt change required for the threshold  $\tau(t)$ , as shown from the purple dots in Fig. 3.

This sudden shift enables us to identify an image-specific threshold for anomaly detection.

To find this abrupt changing point, we first estimate how the threshold changes with respect to iterations. We use a tangent parametric model to model the threshold dynamics, fitting its parameters  $a$  and  $b$  using least squares:

$$\tau(t) = a \tan(bt) \quad (13)$$

This is shown by the red curve in Fig. 3. Using the fitted function  $\tau(t)$ , we obtain a smooth representation of the threshold curve, that can be used to compute its derivative  $\tau'(t)$ . We then define the stopping threshold  $\tau_{stop}$ , which we use in Algorithm 1 to produce the final segmentation mask, as the value corresponding to the rate of change  $\tau'(t)$  that first exceeds a predefined value  $r$ :

$$\text{Find } \tau_{stop} = \tau(t), \text{ such that } \tau'(t) = ab \left( \frac{1}{\cos(bt)} \right)^2 > \gamma \quad (14)$$

### 3.5. Training Process with Spatial Random Masking

Here we discuss the training process of our model. Our goal is to have a reconstruction model that can spatially reconstruct missing areas from the image with high-frequency guidance. To do this, we first synthesize spatially masked images from our training set  $D_{tr} = \{\mathbf{x}^i\}_{i=1}^N$  which is comprised of ‘normal’ in-distribution images. Since there is no anomaly in the training set to mask from, we generate randomly shaped masks with the help of a Gaussian distribution. Firstly, we select a random point in the brain area where  $\mathbf{m}$  is the 3D mask of the brain:  $(\mu_x, \mu_y, \mu_z) \sim \mathbf{m}$  to simulate the center of the anomaly. Then, we generate a multivariate 3D Gaussian distribution with the selected point  $(\mu_x, \mu_y, \mu_z)$  as the center of the distribution of the mask to generate a random shape. The probabilistic density function of the anisotropic 3D Gaussian distribution is

$$p(x, y, z) = \frac{1}{\sqrt{(2\pi)^3 |\Sigma|}} \exp\left(-\frac{1}{2}(\mathbf{r} - \boldsymbol{\mu})^T \Sigma^{-1} (\mathbf{r} - \boldsymbol{\mu})\right) \quad (15)$$

Here,  $\mathbf{r} = [x \ y \ z]^T$  is the position vector, and  $\boldsymbol{\mu} = [\mu_x \ \mu_y \ \mu_z]^T$  denotes the mean vector (center of the distribution). The anisotropic covariance matrix  $\Sigma$  controls the spread and shape of the Gaussian distribution, where  $|\Sigma|$  is its determinant, and  $\Sigma^{-1}$  is its inverse. To ensure the dense region of the Gaussian distribution covers part of the brain but not the entire brain, we sample  $\Sigma$  by drawing eigenvalues  $\lambda_1, \lambda_2, \lambda_3$  uniformly from  $[0.3, 10]$  constructing the covariance matrix using a randomly sampled orthogonal matrix, as follows:

$$\Sigma = O \text{diag}(\lambda_1, \lambda_2, \lambda_3) O^T. \quad (16)$$

The probability density function  $p(x, y, z)$  determines the likelihood of sampling points from the distribution to serve

as part of the masked area. we sample 100,000 points from the corresponding 3D multivariate normal distribution, and these points compose the random shaped mask  $\mathbf{m}_r$ , as illustrated in Fig. 2 (b). To generate masks of varying sizes, the initial masks are upsampled by a factor of up to 4. Sampled points that fall outside the boundaries of the brain mask are discarded to ensure that the mask generated remains within the valid brain region.

After the mask is generated, the input image  $\mathbf{x}$  is corrupted with Gaussian noise  $\epsilon$  in the masked area  $\hat{\mathbf{x}}$  and then fed into the model  $f$ , conditioned on the high-frequency image  $\mathbf{x}_f$  discussed in Section 3.3, for reconstruction.

$$\hat{\mathbf{x}} = \epsilon \odot \mathbf{m}_r + \mathbf{x} \odot (1 - \mathbf{m}_r) \quad (17)$$

$$\mathbf{x}' = f(\hat{\mathbf{x}}, \mathbf{x}_f) \quad (18)$$

The network  $f$  follows a UNet architecture and is trained by minimizing the  $L_2$  distance loss between the reconstructed image and the original image.

$$L = \|\mathbf{x}' - \mathbf{x}\|_2 \quad (19)$$

Building upon (Liang et al., 2024), we employ a single unified model for the entire mask-shrinking process, eliminating the need to separate the first iteration.

## 4. Experiments

### 4.1. Experiment Settings

#### 4.1.1. Dataset

In this section, we will list all the datasets used in this paper. First, we utilize cognitively normal data from the **Open Access Series of Imaging Studies - 3 (OASIS3)** (LaMontagne, Benzinger, Morris, Keefe, Hornbeck, Xiong, Grant, Hassenstab, Moulder, Vlassenko, Raichle, Cruchaga and Marcus, 2019) and the **Alzheimer’s Disease Neuroimaging Initiative (ADNI)** (Alzheimer’s Disease Neuroimaging Initiative (ADNI), 2004) datasets, as they are free from major brain pathologies and artifacts. OASIS includes 755 cognitively normal adults and we used the T2 sequence. The original goal of ADNI’s creation was to test whether serial MRI, PET, biological markers, clinical or psychological assessment can help measure progression of mild cognitive impairment and Alzheimer’s disease. Herein, from ADNI we use only the FLAIR scans from 961 cognitively-normal subjects. From both datasets, 25 subjects are held-out as in-distribution test set for anomaly detection (Sec.4.2, 4.3), while the rest are used as training images.

For evaluating real artifact detection, we test our model on a private dataset acquired at our institution, consisting of 16 subjects scanned with T2-weighted imaging, wherein substantial acquisition artifacts are present. We also use two datasets with brain pathology, specifically **BraTS2021** with glioma cases (Bakas, Akbari, Sotiras, Bilello, Rozycki, Kirby, Freymann, Farahani and Davatzikos, 2017; Baid et al., 2021) and **ISLES2015** (Maier, Menze, Von der Gablentz, Häni, Heinrich, Liebrand, Winzeck, Basit, Bentley, Chen et al., 2017) with stroke lesion cases. We randomly selected 139 samples from BraTS2021 for testing,

**Table 1**

Performance for detecting anomalous synthetic imaging artifacts in 3D scans. Best in bold.

different MRI sequence (T2)							Gaussian noise						
	AUROC	AUPRC	FPR80	FPR90	FNR80	FNR90		AUROC	AUPRC	FPR80	FPR90	FNR80	FNR90
AE	84.8	82.5	27.6	48.3	60.0	84.0	AE	91.8	90.2	10.3	24.1	79.3	79.3
DDPM	78.4	82.0	48.2	55.2	66.7	66.7	DDPM	98.3	98.5	<b>0.0</b>	13.8	13.8	13.8
Auto DDPM	82.3	78.4	17.2	48.2	80.0	80.0	Auto DDPM	76.6	75.0	41.4	51.7	75.9	89.7
Cycl. Unet	<b>100.0</b>	<b>100.0</b>	<b>0.0</b>	<b>0.0</b>	<b>0.0</b>	<b>0.0</b>	Cycl. Unet	<b>100.0</b>	<b>100.0</b>	<b>0.0</b>	<b>0.0</b>	<b>0.0</b>	<b>0.0</b>
DAE	<b>100.0</b>	<b>100.0</b>	<b>0.0</b>	<b>0.0</b>	<b>0.0</b>	<b>0.0</b>	DAE	<b>100.0</b>	<b>100.0</b>	<b>0.0</b>	<b>0.0</b>	<b>0.0</b>	<b>0.0</b>
IterMask3D	<b>100.0</b>	<b>100.0</b>	<b>0.0</b>	<b>0.0</b>	<b>0.0</b>	<b>0.0</b>	IterMask3D	<b>100.0</b>	<b>100.0</b>	<b>0.0</b>	<b>0.0</b>	<b>0.0</b>	<b>0.0</b>
chunk missing (middle)							periodic line artifact						
	AUROC	AUPRC	FPR80	FPR90	FNR80	FNR90		AUROC	AUPRC	FPR80	FPR90	FNR80	FNR90
AE	44.9	54.4	86.2	96.6	75.9	89.7	AE	79.8	83.2	27.6	86.2	82.8	44.8
DDPM	60.5	56.5	65.5	82.8	79.3	89.7	DDPM	99.5	99.6	<b>0.0</b>	<b>0.0</b>	34.5	34.5
Auto DDPM	61.4	57.6	51.7	55.2	79.3	89.7	Auto DDPM	<b>100.0</b>	<b>100.0</b>	<b>0.0</b>	<b>0.0</b>	<b>0.0</b>	<b>0.0</b>
Cycl. Unet	45.9	48.6	79.3	89.7	65.5	89.7	Cycl. Unet	99.4	99.4	<b>0.0</b>	3.4	17.2	17.2
DAE	61.7	61.3	55.2	82.8	72.4	89.7	DAE	93.1	91.2	10.3	10.3	79.3	79.3
IterMask3D	<b>99.6</b>	<b>99.6</b>	<b>3.4</b>	<b>3.4</b>	<b>10.3</b>	<b>10.3</b>	IterMask3D	97.3	97.6	<b>0.0</b>	1.7	17.2	17.2
ring artifact							chunk missing (top)						
	AUROC	AUPRC	FPR80	FPR90	FNR80	FNR90		AUROC	AUPRC	FPR80	FPR90	FNR80	FNR90
AE	67.4	69.6	58.6	86.2	58.6	89.7	AE	44.8	51.4	86.2	96.6	79.3	89.7
DDPM	99.5	99.5	<b>0.0</b>	3.4	10.3	10.3	DDPM	59.3	60.9	62.1	86.2	<b>79.3</b>	<b>79.3</b>
Auto DDPM	<b>99.9</b>	<b>99.9</b>	<b>0.0</b>	<b>0.0</b>	<b>3.4</b>	<b>3.4</b>	Auto DDPM	69.2	64.8	<b>37.9</b>	<b>55.2</b>	75.9	86.2
Cycl. Unet	93.6	88.8	6.9	20.7	31.0	31.0	Cycl. Unet	54.6	51.9	69.0	75.9	<b>79.3</b>	89.7
DAE	92.9	90.8	10.3	13.8	79.3	79.3	DAE	52.8	54.9	75.9	82.8	<b>79.3</b>	86.2
IterMask3D	99.3	99.3	<b>0.0</b>	3.4	10.3	10.3	IterMask3D	<b>76.8</b>	<b>81.0</b>	<b>37.9</b>	96.6	<b>79.3</b>	<b>79.3</b>

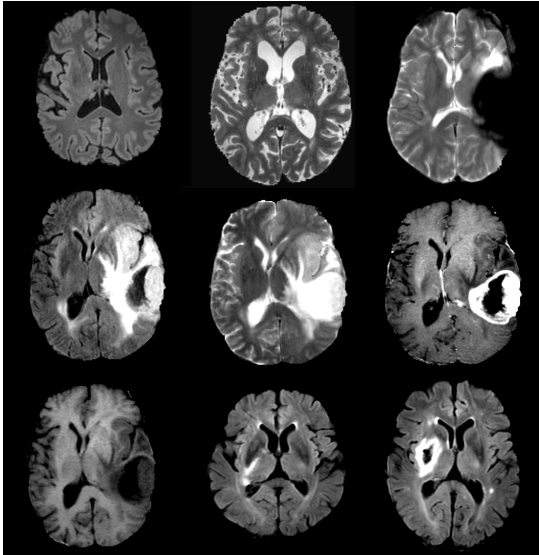


**Figure 4:** Illustration of the datasets used in the format: dataset name (sequence). First row, left to right, ADNI (FLAIR), OASIS (T2), Private Artifact dataset (T2); Second row, left to right, BraTS (FLAIR), BraTS (T2), BraTS (T1ce); Third row, left to right, BraTS (T1), ISLES (FLAIR) (with small lesion), ISLES (FLAIR) (with big lesion).

following the same testing sample selection as (Liang et al., 2024, 2023). For ISLES2015, we used all 28 cases. During evaluation, if multiple lesion classes are provided, they are merged into a single class.

For experiments on 2D slices, we follow the same data pre-processing and selection process as described in (Liang et al., 2023). For 3D images, we first crop the image to a uniform size of  $[192, 192, 192]$ , with the brain at the center of the image. Next, we perform resampling to ensure a standardized voxel size spacing of  $[1, 1, 1]$ . Skull-stripping is then applied using Robex (Iglesias, Liu, Thompson and

Tu, 2011) to extract the brain region from the image. Finally, to exclude outliers and standardize image intensity distributions across subjects, we apply an iterative z-score normalization process constrained to the brain region. After initial z-score normalization of the brain area, we recompute the mean and variance using only pixels with intensities within two standard deviations of the current distribution to reduce effect of outliers in the statistics, and re-normalize. This step is repeated three more times.

#### 4.1.2. Implementation Details

For experiments on 2D slices we adopt as backbone model the network architecture from (Liang et al., 2024). As a 3D model we utilize a UNet with the same structure as (Xu, Moffat, Seale, Liang, Wagner, Whitehouse, Menon, Newcombe, Voets, Banerjee et al., 2024). The 2D model is trained with Adam optimizer with  $1e^{-4}$  learning rate for 8000 iterations with a batch size of 32. The 3D model is trained using the Adam optimizer with a learning rate of  $1e^{-3}$  for 200 epochs and a batch size of 2. The hyperparameter of the model  $\gamma$  is set to 0.01 for pathology detection, and we increase it to 0.05 for 3D pathology segmentation to get a more accurate segmentation map. For 2D pathology segmentation,  $\gamma$  is set to 0.01 because intensity normalization of 2D slices results to different intensity range.  $r$  for frequency masking is set to 15. For fair comparison, all baselines are implemented with the same backbone network. Experiments were implemented in PyTorch and training performed using one Nvidia V100 GPU with 24GB memory. Data augmentation is applied with random rotation at a probability of 0.1. No post-processing is used to refine the segmentation.

#### 4.1.3. Baselines

We include both reconstruction-based and non-reconstruction-based methods for baseline comparisons. Reconstruction-based approaches follow the ‘corrupt-and-reconstruct’ paradigm

and we include the standard autoencoder (denoted **AE**), which applies compression as corruption (Baur et al., 2021), as well as diffusion-based methods (Pinaya et al., 2022a; Bercea et al., 2023a), which use additive noise as the corruption mechanism. Among non-reconstruction-based methods, we evaluate a cross-sequence translation model (**Cyclic UNet**) (Liang et al., 2023), a transformer-based method with VQ-VAE (**Transformer**) (Pinaya et al., 2022b) and a denoising autoencoder (**DAE**) (Kascenas et al., 2022).

We implement AE, Cyclic UNet, and DAE using 3D architectures. For diffusion-based methods, since no 3D implementations are available, we implement them in 2D and apply them slice-by-slice on 3D volumes; final evaluation metrics are computed in 3D. For the Transformer model, we report the results directly from the original paper (Pinaya et al., 2022b) because the code is not publicly available for reproducibility.

#### 4.2. Synthetic Artifact Detection on 3D Images

We first evaluate performance of our model for detecting artifacts that may appear as unexpected anomalies during deployment. Methods for detecting unexpected artifacts during acquisition are useful for implementing quality-assurance frameworks. It is often difficult to annotate precise ground truth segmentation labels for artifacts, particularly when they manifest as global patterns across the entire image. Additionally, image-level detection is typically sufficient for identifying such anomalies. Therefore we evaluate performance based on artifact detection rather than segmentation.

We begin by testing the model’s ability to detect synthetic artifacts. We train models on cognitively normal data from ADNI using the FLAIR sequence, which contain no pathology or artifacts. This defines the in-distribution normal data. To evaluate anomaly detection, we first assess the model’s ability to detect scans of a different sequence, T2 (anomalies far from the training distribution). Then, we simulate various types of anomalies (anomalies closer to the training distribution) by generating images with missing chunks in the middle or top regions of the brain, adding Gaussian noise, or introducing circular and linear artifacts, as illustrated in Fig. 5 (The predicted anomaly map is overlaid in red on the image). Some artifacts follow the anomaly generation method described in (Graham, Tudosiu, Wright, Pinaya, Teikari, Patel, U-King-Im, Mah, Teo, Jäger et al., 2023). The simulated anomalies are added to FLAIR from the ADNI validation set, while the original, unaltered images are used as in-distribution normal control samples for performance evaluation.

When evaluating the performance, we adopt two threshold-independent metrics: the Area Under the Receiver Operating Characteristic Curve (AUROC) and Area Under the Precision-Recall Curve (AUPRC). We assign a label of 0 to ‘normal’ in-distribution samples and a label of 1 to anomalous samples. For all baselines, the anomaly score of each image is computed as the mean value of the error map between the input image and its final reconstruction. For IterMask3D, the anomaly score for each image is the

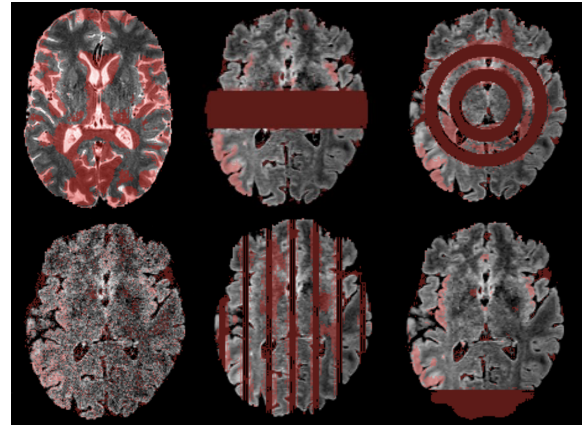


**Figure 5:** Visualization of anomaly detection results on images with synthetic anomalies using our method *IterMask3D*. The final anomaly map is overlaid in red on the original image containing the artifact.

number of pixels (voxels) of the final mask. In addition, we provide several supplementary metrics to further evaluate performance at specific sensitivity levels: We compute the false positive rates (FPR) for anomalous samples, given that the true positive rates (TPR) for correctly identifying in-distribution samples are fixed at 80% and 90%. We refer to these metrics as FPR80 and FPR90, respectively. Correspondingly, we measure the false negative rates (FNR) for in-distribution samples when setting the TPR at 80% (FNR80) and 90% (FNR90).

Results are shown in Table. 1. When testing on MRI sequences significantly different from the training distribution or introducing global anomalies such as Gaussian noise, most reported methods effectively distinguish these anomalies from in-distribution samples. However, baseline methods typically exhibit reduced performance when faced with large missing brain regions, particularly in cases where chunks from the top or middle areas of the brain are absent. Reconstruction-based approaches generally corrupt the input images and attempt to restore the missing information, but these methods are usually trained to reconstruct only partially corrupted regions, relying heavily on surrounding contextual information. Consequently, when a substantial portion of the brain is missing—visually resembling the background (e.g. air)—these methods often fail to reconstruct meaningful structures, resulting in low reconstruction errors and undetected anomalies.

On the other hand, when the missing areas are small and lead to structural discontinuities, such as line or ring artifacts, baseline methods with strong generative capabilities, such as diffusion-based models, can successfully reconstruct these anomalies using nearby information, thereby enabling their detection.

In contrast, our proposed method incorporates high-frequency structural information as additional guidance. This high-frequency component captures global structural patterns across the entire image, enhancing sensitivity to structural inconsistencies. As a result, our method achieves

**Table 2**

Detection of real-world imaging artifacts in 3D scans. Best in bold.

	AUROC	AUPRC	FPR80	FPR90	FNR80	FNR90
AE	41.9	38.1	76.0	92.0	80.0	80.0
DDPM	45.8	40.4	63.3	100.0	80.0	86.7
Auto DDPM	55.3	45.6	66.7	66.7	73.3	86.7
Cycl. Unet	83.2	75.8	20.0	52.0	80.0	80.0
DAE	99.2	<b>99.6</b>	<b>0.0</b>	<b>0.0</b>	<b>6.7</b>	<b>6.7</b>
IterMask3D	<b>99.7</b>	<b>99.6</b>	<b>0.0</b>	<b>0.0</b>	<b>6.7</b>	<b>6.7</b>

robust anomaly detection performance, effectively identifying anomalies characterized both by large missing anatomical regions and small localized discontinuities.

### 4.3. Real-world Artifact Detection on 3D Images

In this section, we evaluate our model’s performance on real-world imaging artifacts in T2 MRI sequence, obtained from our collaborating hospital. Artifacts in our database are primarily metallic susceptibility artefacts, which are reasonably common in MRI scans of the brain due to implanted medical devices such as programmable VP-shunt valves or cochlear implant devices. Examples are shown in Fig. 4 (first row, third image) and Fig. 6. Typically, these artifacts feature a missing brain region covered by hypo-intense signal in T2, accompanied by hyper-intense signal spikes at the boundary of the affected area. All models were trained exclusively on cognitively normal cases from the OASIS dataset in the T2 sequence. For testing purposes, we combined our private artifact dataset with the held-out T2 test samples from OASIS and ADNI without artifacts and evaluated performance using the following metrics: AUROC, AUPRC, FPR80, FPR90, FNR80, and FNR90. All methods tested use the mean value of the error map as anomaly score during evaluation.

The quantitative results, shown in Table. 2, demonstrate promising performance for our method and comparable with the DAE baseline. However, upon visual inspection of anomaly maps (shown in Fig.6), we observe substantial qualitative differences between the two methods. As illustrated in the top row of Fig.6, the DAE method primarily detects hyper-intense regions near the anomaly, also including parts of normal brain tissue, but fails entirely to identify the main artifact region that appears hypo-intense, as structural discontinuity of the brain. This limitation arises because DAE has to assume a prior about the appearance of anomalies, reflected in the use of hyper-intense noise for its training; hence, it predominantly targets and removes high-intensity signals during testing, missing artifacts with low intensity value. In comparison, as shown in the bottom row of Fig. 6, our method makes no strong prior assumptions about the appearance of anomalies and can identify both hypo-intense and hyper-intense artifacts, including areas with signal loss and bright boundary spikes. This allows our method to detect structural discontinuities more effectively than DAE.

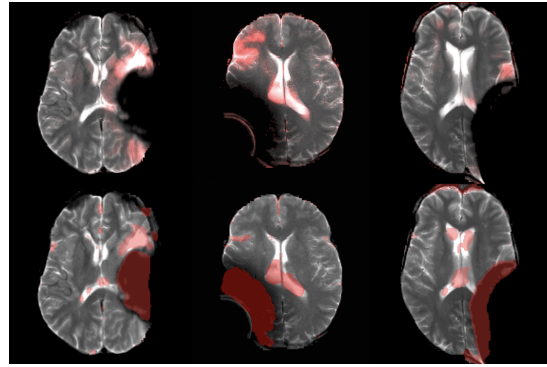


**Figure 6:** Visualization of artifact detection results on our private dataset using DAE (Kascenas et al., 2022) (top row) and our method *IterMask3D* (bottom row). The final anomaly map is overlaid in red on the original image. DAE is shown to detect the hyper-intense area (mostly in normal brain area) as anomaly, while our method better detects the actual anomalous artifact.

### 4.4. Pathology Segmentation on 2D Slices of Scans

In this section, we evaluate performance of pathology segmentation on 2D MRI slices. We follow standard practices in the field (Pinaya et al., 2022a; Bercea et al., 2023a) to ensure a fair comparison, where the model is trained on normal 2D slices (i.e., healthy in this experiment) extracted from 3D scans of training subjects and tested on 2D slices with pathologies extracted from 3D scans of test subjects from the same database. Anomaly segmentation performance was evaluated by how well the model is able to segment the previously unseen pathological regions. The metrics used in this experiment are Dice coefficient (DSC), sensitivity, precision, and Structural Similarity Index Measure (SSIM). Dice, sensitivity, and precision are used to evaluate segmentation performance, where Dice reflects the overall segmentation accuracy, while higher sensitivity indicates fewer false negatives, and higher precision corresponds to fewer false positives. SSIM is used to measure the structural similarity between the input image and the reconstructed image within the ‘normal’ brain regions, demonstrating the model’s ability to accurately reconstruct in-distribution tissue and thereby reduce false positives.

We test on all sequences of BraTS to show the model is robust to different sequences with pathologies of different intensities. Results are shown in Table 3. *IterMask<sup>2</sup>* is our previously proposed 2D method, and we integrate the newly proposed subject-specific thresholding strategy into our original 2D method, eliminating the need for validation data, denoted as *IterMask<sup>2</sup> + thres*. The enhanced method achieves better or comparable performance, demonstrating the effectiveness of the proposed thresholding approach. The results show that our model performs consistently well across different sequences under different evaluation metrics, demonstrating promising generalizability.

Here, we also conduct a detailed analysis of the baseline model DAE (Kascenas et al., 2022) on the BraTS sequences. This model is trained to remove added noise

**Table 3**

Performance of methods for pathology segmentation on 2D slices across all MRI sequences in BraTS. Best in bold.

sequence	FLAIR				T1CE				T2				T1			
	DSC	Sens	Prec	SSIM												
AE	33.4	54.0	27.0	0.941	32.3	50.1	26.4	0.957	30.2	62.8	21.1	0.937	28.5	<b>94.9</b>	17.4	0.953
DDPM	60.7	57.8	69.8	0.980	37.9	35.2	46.2	0.984	36.4	33.6	44.2	0.984	29.4	32.1	31.5	0.977
AutoDDPM	55.5	57.5	58.7	0.937	36.9	58.9	28.9	0.903	29.7	53.0	22.3	0.907	33.5	61.1	24.7	0.910
Cycl.UNet	65.0	63.4	73.9	0.864	42.6	47.5	42.9	0.923	49.5	48.8	53.4	0.831	37.0	45.8	35.2	0.926
DAE_pos	79.7	79.1	<b>84.5</b>	0.926	36.7	42.0	36.2	0.844	69.6	68.1	<b>75.3</b>	0.903	29.5	61.2	20.5	0.860
DAE_neg	28.5	<b>94.9</b>	17.3	0.875	34.7	37.9	39.3	0.966	28.5	<b>94.9</b>	17.4	0.885	47.9	53.7	50.9	0.958
DAE_full	73.7	72.9	80.5	0.926	46.3	47.9	51.5	0.969	60.4	58.5	69.1	0.897	44.5	48.0	47.5	0.964
IterMask2	80.2	81.3	83.3	<b>0.985</b>	61.7	59.1	<b>70.9</b>	<b>0.997</b>	71.2	74.4	72.9	<b>0.994</b>	58.5	56.6	<b>67.6</b>	<b>0.996</b>
IterMask2+thres	<b>80.4</b>	80.6	83.1	0.983	<b>64.3</b>	<b>62.6</b>	69.8	0.996	<b>71.4</b>	72.2	72.0	0.991	<b>59.6</b>	57.7	<b>67.6</b>	<b>0.996</b>

and, during testing, treats anomalies as if they were noise to be removed. The original DAE adds hyper-intense noise — clipped to positive values ( $[0, +\infty]$  row in the table), and shows strong performance on FLAIR (Dice: 0.797) and T2 (Dice: 0.696), but performs poorly on T1 (Dice: 0.295) and T1ce (Dice: 0.367). As shown in Fig. 4, tumors in the BraTS dataset appear hyper-intense in FLAIR and T2, dark in T1, and contain both hyper-intense and dark regions in T1ce. For analysis, we change the noise to the negative range ( $[-\infty, 0]$  as in table). Then, performance on T1 improves to 0.479. If the noise includes both positive and negative values ( $[-\infty, +\infty]$ ), performance on T1ce improves to 0.463. These results suggest that DAE requires prior knowledge about the expected anomaly appearance to perform well, which is usually unavailable when the types of anomalies to expect is unknown prior to deployment. In comparison, our method consistently achieves better or comparable performance to DAE without relying on intensity priors, demonstrating its effectiveness.

#### 4.5. Pathology Segmentation on 3D Scans

In this section, we test the performance on whole 3D scans and aim to segment pathologies as anomalies. The models are trained using cognitively normal subjects from the ADNI and OASIS datasets as described in section 4.1.1. We test the models on FLAIR and T2 sequences of BraTS, as well as FLAIR of the ISLES2015 dataset.

We assess segmentation performance using several metrics: Dice coefficient (DSC), AUROC, sensitivity, precision, Jaccard index, and Average Symmetric Surface Distance (ASSD). Additionally, we compute the Peak Signal-to-Noise Ratio (PSNR) within the healthy brain regions (excluding pathology) to evaluate the model’s ability to accurately reconstruct in-distribution, normal tissue.

Results are presented in Table 4. Our method outperforms all baseline approaches that do not rely on prior knowledge of anomaly appearance during training. In particular, on the FLAIR sequence of the BraTS dataset, our model shows clear improvements over AE, DDPM, AutoDDPM, Cyclic UNet, and Transformer-based method. For the DAE baseline, the original implementation uses noise with 0.2 standard deviation, and due to the altered range of intensities in our data from z-score normalization, we rescale it to the corresponding 1.2 standard deviations. For

**Table 4**

Performance for 3D pathology segmentation in BraTS and ISLES datasets. Best in bold.

BraTS FLAIR							
	DSC	AUC	Sensitivity	Precision	Jaccard	PSNR	ASSD
AE	16.0	92.6	42.8	10.7	8.9	29.1	17.4
DDPM	28.5	95.7	55.4	23.5	18.9	31.3	13.3
Auto DDPM	21.5	80.7	27.9	21.6	12.7	26.8	16.9
Cycl. UNet	40.0	96.9	45.9	39.5	28.3	13.5	26.3
Transformer	61.7	-	-	-	-	-	-
DAE (1.2std)	36.6	96.7	47.9	35.9	23.3	<b>37.2</b>	14.3
DAE (3std)	66.7	99.1	71.1	68.7	52.5	34.5	6.2
IterMask3D	<b>69.7</b>	<b>99.2</b>	<b>72.7</b>	<b>71.1</b>	<b>56.7</b>	32.2	<b>5.1</b>
BraTS T2							
	DSC	AUC	Sensitivity	Precision	Jaccard	PSNR	ASSD
AE	12.4	90.5	66.1	7.1	6.8	17.7	30.7
DDPM	18.9	92.8	42.6	14.1	11.6	35.6	16.2
Auto DDPM	19.4	77.8	29.4	16.2	11.1	27.2	18.13
Cycl. UNet	20.2	93.6	47.3	13.7	11.8	26.5	17.7
DAE (1.2std)	31.7	96.4	56.0	24.7	19.6	<b>39.4</b>	15.6
DAE (3std)	53.6	<b>97.9</b>	<b>57.0</b>	<b>56.4</b>	38.3	1.0	<b>9.5</b>
IterMask3D	<b>53.8</b>	97.7	55.4	55.9	<b>39.6</b>	36.7	<b>9.5</b>
ISLES FLAIR							
	DSC	AUC	Sensitivity	Precision	Jaccard	PSNR	ASSD
AE	7.4	93.3	53.3	4.8	4.1	26.9	24.5
DDPM	12.1	95.2	<b>58.5</b>	9.4	7.9	30.4	21.7
Auto DDPM	6.94	82.6	45.7	5.1	4.1	24.15	25.17
Cycl. UNet	15.1	94.9	32.8	12.8	9.7	24.1	24.3
DAE (1.2std)	20.9	97.3	38.7	22.5	12.6	<b>34.4</b>	23.8
DAE (3std)	<b>33.0</b>	<b>97.8</b>	42.4	<b>33.2</b>	<b>24.1</b>	32.0	21.7
IterMask3D	31.4	97.2	40.3	30.4	23.0	29.3	<b>20.3</b>

an even stronger comparison, we further tune DAE’s noise level to 3 standard deviations, value found via configuration experiments aiming to maximize its performance on the test set. Although this gives it an edge over our method, as it is a form of overfitting the test set, it optimally matches the DAE’s intensity prior to these anomalies and gives an indication about its optimal potential. Both DAE configurations are reported in Table 4 as DAE (1.2std) and DAE (3std). Notably, our method achieves comparable performance to the over-tuned DAE(3std), despite not incorporating any intensity-based prior knowledge.

#### 4.6. Ablation Study

Finally, we conduct ablation studies to evaluate the effectiveness of spatial masking and frequency masking. Ablation experiments are repeated using both 2D and 3D models for the task of pathology segmentation, as described in the

**Table 5**  
Ablation study of spatial and frequency masking strategies.

2D BraTS FLAIR			
	DSC	Sensitivity	Precision
frequency masking only	0.751	0.738	0.796
spatial masking only	0.642	0.694	0.636
IterMask <sup>2</sup>	0.802	0.813	0.833
3D BraTS FLAIR			
frequency masking only	0.608	0.659	0.648
spatial masking only	0.404	0.437	0.422
Itermask3D	0.697	0.727	0.711

previous two sections, using the FLAIR sequence of the BraTS dataset. Results are shown in Table 5. To evaluate the role of spatial masking, we remove the spatial mask refinement process and input only the high-frequency structural information to the network. The anomaly score is then computed from a single-step reconstruction, denoted as *frequency masking only* in Table 5. Next, to evaluate the impact of frequency masking, we remove the high-frequency-based auxiliary input and train the model using only spatially masked images as input. The full iterative reconstruction process is retained, but without high-frequency structural guidance. Results for this variant are reported as *spatial masking only* in Table 5. Results in all settings demonstrate the positive contribution of both components.

#### 4.7. Discussion and Limitations

Reconstruction-based anomaly detection methods typically rely on the reconstruction error map to identify anomalous regions, using a threshold to differentiate anomalies from normal tissue. However, a common limitation of these methods is their reduced sensitivity to anomalies that produce only subtle reconstruction errors. And in the context of 3D model training and evaluation, an inherent challenge that makes this issue worse is the inevitable domain gap between training and testing datasets. It is often impractical to train the model on data obtained from the exact same imaging center or scanner as the testing data. Although our iterative mask refinement approach progressively reduces this domain gap by iteratively exposing to the model larger regions from the test image at inference time, anomalies that generate reconstruction errors similar to those caused by domain shifts can be mistakenly considered normal. Consequently, these anomalies may become unmasked and remain undetected during the iterative process.

Moreover, medical imaging data, especially MRI, differ significantly from natural images in terms of intensity range variability. While natural images typically have a fixed intensity range (e.g., 0–255 or 0–1), intensity ranges in MRI images exhibit substantial variability across datasets, scanners and acquisition protocols, as MRI intensity units are not standardized. Large intensity shift due to this between the training and test distribution can lead to suboptimal behavior of anomaly segmentation methods. A related challenge is the normalization of medical image intensities, which aims to assign comparable intensity ranges to the same tissue across

images, ensuring that intensity shifts do not negatively affect reconstruction accuracy and anomaly detection.

## 5. Conclusion

This work has presented IterMask3D, an unsupervised anomaly segmentation framework developed for 3D brain MRI. By introducing an **iterative spatial mask refinement** strategy combined with **high-frequency structural guidance**, IterMask3D effectively detects reconstruction errors in anomalous regions while minimizing false positives in normal tissue. Additionally, we proposed a **subject-specific thresholding strategy** enabling adaptive anomaly detection without dependence on external in-distribution validation datasets.

Through extensive evaluations on various datasets, including synthetic and real-world imaging artifacts, as well as multiple brain pathologies across MRI sequences, IterMask3D consistently demonstrated superior or competitive performance compared to previous methods. Results demonstrate particularly promising performance for detection of imaging artifacts which could be of practical usefulness for quality-assurance in imaging workflows. Results on unsupervised pathology segmentation, although achieving state-of-the-art for unsupervised segmentation, they still have room for improvement towards levels achievable by supervised segmentation methods. The improvement demonstrated by this method, however, shows there is substantial potential in unsupervised anomaly segmentation that is still untapped. Given that this category of methods could unlock applications for which supervised methods is less appropriate, such as segmentation of any type of brain lesion or incidental findings, we hope this study will motivate further future research in this direction.

## Acknowledgments

For this work, ZL is supported by a scholarship provided by the EPSRC Doctoral Training Partnerships programme [EP/W524311/1]. YI is supported by the EPSRC Centre for Doctoral Training in Health Data Science (EP/S02428X/1). The authors also acknowledge UKRI grant reference [EP/X040186/1] and EPSRC grant [EP/T028572/1]. NLV gratefully acknowledges support from the NIHR Oxford Health Biomedical Research Centre [NIHR203316]. The views expressed are those of the author(s) and not necessarily those of the NIHR or the Department of Health and Social Care. The Wellcome Centre for Integrative Neuroimaging is supported by core funding from the Wellcome Trust (203139/Z/16/Z and 203139/A/16/Z). The authors also acknowledge the use of the University of Oxford Advanced Research Computing (ARC) facility in carrying out this work (<http://dx.doi.org/10.5281/zenodo.22558>).

Data used in preparation of this article were obtained from the Alzheimer’s Disease Neuroimaging Initiative (ADNI) database ([adni.loni.usc.edu](http://adni.loni.usc.edu)). As such, the investigators within the ADNI contributed to the design and implementation of ADNI and/or provided data but did not participate in

analysis or writing of this report. A complete listing of ADNI investigators can be found at: [https://adni.loni.usc.edu/wp-content/uploads/how\\_to\\_apply/ADNI\\_Acknowledgement\\_List.pdf](https://adni.loni.usc.edu/wp-content/uploads/how_to_apply/ADNI_Acknowledgement_List.pdf). Data collection and sharing for this project were funded by the Alzheimer’s Disease Neuroimaging Initiative (ADNI) (National Institutes of Health Grant U01 AG024904) and DOD ADNI (Department of Defense award number W81XWH-12-2-0012). ADNI is funded by the National Institute on Aging, the National Institute of Biomedical Imaging and Bioengineering, and through generous contributions from the following: AbbVie, Alzheimer’s Association, Alzheimer’s Drug Discovery Foundation, Araclon Biotech, BioClinica, Inc., Biogen, Bristol-Myers Squibb Company, CereSpir, Inc., Cogstate, Eisai Inc., Elan Pharmaceuticals, Inc., Eli Lilly and Company, EuroImmun, F. Hoffmann-La Roche Ltd and its affiliated company Genentech, Inc., Fujirebio, GE Healthcare, IXICO Ltd., Janssen Alzheimer Immunotherapy Research & Development, LLC., Johnson & Johnson Pharmaceutical Research & Development LLC., Lumosity, Lundbeck, Merck & Co., Inc., Meso Scale Diagnostics, LLC., NeuroRx Research, Neurotrack Technologies, Novartis Pharmaceuticals Corporation, Pfizer Inc., Piramal Imaging, Servier, Takeda Pharmaceutical Company, and Transition Therapeutics. The Canadian Institutes of Health Research provide funds to support ADNI clinical sites in Canada. Private sector contributions are facilitated by the Foundation for the National Institutes of Health ([www.fnih.org](http://www.fnih.org)). The grantee organization is the Northern California Institute for Research and Education, and the study is coordinated by the Alzheimer’s Therapeutic Research Institute at the University of Southern California. ADNI data are disseminated by the Laboratory for Neuroimaging at the University of Southern California.

Data were provided in part by OASIS [OASIS-3: Longitudinal Multimodal Neuroimaging: Principal Investigators: T. Benzinger, D. Marcus, J. Morris; NIH P30 AG066444, P50 AG00561, P30 NS09857781, P01 AG026276, P01 AG003991, R01 AG043434, UL1 TR000448, R01 EB009352. AV-45 doses were provided by Avid Radiopharmaceuticals, a wholly owned subsidiary of Eli Lilly.]

For the purpose of open access, the authors have applied a creative commons attribution (CC BY) licence (where permitted by UKRI, ‘open government licence’ or ‘creative commons attribution no-derivatives (CC BY-ND) licence’ may be stated instead) to any author accepted manuscript version arising.

During the preparation of this work the authors used ChatGPT to improve writing and grammar. After using this tool, the authors reviewed and edited the content as needed and take full responsibility for the content of the publication.

## References

- Alzheimer’s Disease Neuroimaging Initiative (ADNI), 2004. Alzheimer’s disease neuroimaging initiative. URL: <http://adni.loni.usc.edu/>.
- Atlason, H.E., Love, A., Sigurdsson, S., Gudnason, V., Ellingsen, L.M., 2019. Unsupervised brain lesion segmentation from mri using a convolutional autoencoder, in: Medical Imaging 2019: Image Processing, SPIE. pp. 372–378.
- Baid, U., Ghodasara, S., Mohan, S., Bilello, M., Calabrese, E., Colak, E., Farahani, K., Kalpathy-Cramer, J., Kitamura, F.C., Pati, S., et al., 2021. The rsna-asnr-miccai brats 2021 benchmark on brain tumor segmentation and radiogenomic classification. arXiv preprint arXiv:2107.02314.
- Bakas, S., Akbari, H., Sotiras, A., Bilello, M., Rozycki, M., Kirby, J.S., Freymann, J.B., Farahani, K., Davatzikos, C., 2017. Advancing the cancer genome atlas glioma mri collections with expert segmentation labels and radiomic features. *Scientific data* 4, 1–13.
- Baur, C., Denner, S., Wiestler, B., Navab, N., Albarqouni, S., 2021. Autoencoders for unsupervised anomaly segmentation in brain mr images: a comparative study. *Medical Image Analysis* 69, 101952.
- Bercea, C.I., Neumayr, M., Rueckert, D., Schnabel, J.A., 2023a. Mask, stitch, and re-sample: Enhancing robustness and generalizability in anomaly detection through automatic diffusion models. arXiv preprint arXiv:2305.19643.
- Bercea, C.I., Rueckert, D., Schnabel, J.A., 2023b. What do aes learn? challenging common assumptions in unsupervised anomaly detection, in: International Conference on Medical Image Computing and Computer-Assisted Intervention, Springer. pp. 304–314.
- Cai, Y., Chen, H., Cheng, K.T., 2024. Rethinking autoencoders for medical anomaly detection from a theoretical perspective, in: International Conference on Medical Image Computing and Computer-Assisted Intervention, Springer. pp. 544–554.
- Chappell, M., 2019. Principles of Medical Imaging for Engineers. Springer International Publishing.
- Graham, M.S., Tudosiu, P.D., Wright, P., Pinaya, W.H.L., Teikari, P., Patel, A., U-King-Im, J.M., Mah, Y.H., Teo, J.T., Jäger, H.R., et al., 2023. Latent transformer models for out-of-distribution detection. *Medical Image Analysis* 90, 102967.
- Hendriks, J., Mutsaerts, H.J., Joules, R., Peña-Nogales, Ó., Rodrigues, P.R., Wolz, R., Burchell, G.L., Barkhof, F., Schranke, A., 2024. A systematic review of (semi-) automatic quality control of t1-weighted mri scans. *Neuroradiology* 66, 31–42.
- Ho, J., Jain, A., Abbeel, P., 2020. Denoising diffusion probabilistic models. *Advances in neural information processing systems* 33, 6840–6851.
- Iglesias, J.E., Liu, C.Y., Thompson, P.M., Tu, Z., 2011. Robust brain extraction across datasets and comparison with publicly available methods. *IEEE transactions on medical imaging* 30, 1617–1634.
- Isensee, F., Jäger, P.F., Full, P.M., Vollmuth, P., Maier-Hein, K.H., 2021. nnu-net for brain tumor segmentation, in: Brainlesion: Glioma, Multiple Sclerosis, Stroke and Traumatic Brain Injuries: 6th International Workshop, BrainLes 2020, Held in Conjunction with MICCAI 2020, Lima, Peru, October 4, 2020, Revised Selected Papers, Part II 6, Springer. pp. 118–132.
- Kamnitsas, K., Ledig, C., Newcombe, V.F., Simpson, J.P., Kane, A.D., Menon, D.K., Rueckert, D., Glocker, B., 2017. Efficient multi-scale 3d cnn with fully connected crf for accurate brain lesion segmentation. *Medical image analysis* 36, 61–78.
- Kascenas, A., Pugeault, N., O’Neil, A.Q., 2022. Denoising autoencoders for unsupervised anomaly detection in brain mri, in: International Conference on Medical Imaging with Deep Learning, PMLR. pp. 653–664.
- Khader, F., Müller-Franzes, G., Tayebi Arasteh, S., Han, T., Haarbuerger, C., Schulze-Hagen, M., Schad, P., Engelhardt, S., Baeßler, B., Foersch, S., et al., 2023. Denoising diffusion probabilistic models for 3d medical image generation. *Scientific Reports* 13, 7303.
- LaMontagne, P.J., Benzinger, T.L., Morris, J.C., Keefe, S., Hornbeck, R., Xiong, C., Grant, E., Hassenstab, J., Moulder, K., Vlassenko, A., Raichle, M.E., Cruchaga, C., Marcus, D., 2019. Oasis-3: Longitudinal neuroimaging, clinical, and cognitive dataset for normal aging and alzheimer disease. medRxiv doi:10.1101/2019.12.13.19014902.
- Liang, Z., Anthony, H., Wagner, F., Kamnitsas, K., 2023. Modality cycles with masked conditional diffusion for unsupervised anomaly segmentation in mri, in: International Conference on Medical Image Computing and Computer-Assisted Intervention, Springer. pp. 168–181.
- Liang, Z., Guo, X., Noble, J.A., Kamnitsas, K., 2024. Itermask 2: Iterative unsupervised anomaly segmentation via spatial and frequency masking

- for brain lesions in mri, in: International Conference on Medical Image Computing and Computer-Assisted Intervention, Springer. pp. 339–348.
- Maier, O., Menze, B.H., Von der Gablentz, J., Häni, L., Heinrich, M.P., Liebrand, M., Winzeck, S., Basit, A., Bentley, P., Chen, L., et al., 2017. Isles 2015-a public evaluation benchmark for ischemic stroke lesion segmentation from multispectral mri. *Medical image analysis* 35, 250–269.
- Oppenheim, A., Lim, J., Kopec, G., Pohlig, S., 1979. Phase in speech and pictures, in: ICASSP'79. IEEE International Conference on Acoustics, Speech, and Signal Processing, IEEE. pp. 632–637.
- Oppenheim, A.V., Lim, J.S., 1981. The importance of phase in signals. *Proceedings of the IEEE* 69, 529–541.
- Pawlowski, N., Lee, M.C., Rajchl, M., McDonagh, S., Ferrante, E., Kamnitsas, K., Cooke, S., Stevenson, S., Khetani, A., Newman, T., et al., 2018. Unsupervised lesion detection in brain ct using bayesian convolutional autoencoders .
- Pinaya, W.H., Graham, M.S., Gray, R., Da Costa, P.F., Tudosiu, P.D., Wright, P., Mah, Y.H., MacKinnon, A.D., Teo, J.T., Jager, R., et al., 2022a. Fast unsupervised brain anomaly detection and segmentation with diffusion models, in: International Conference on Medical Image Computing and Computer-Assisted Intervention, Springer. pp. 705–714.
- Pinaya, W.H., Tudosiu, P.D., Gray, R., Rees, G., Nachev, P., Ourselin, S., Cardoso, M.J., 2022b. Unsupervised brain imaging 3d anomaly detection and segmentation with transformers. *Medical Image Analysis* 79, 102475.
- Rowley, P., Paukner, M., Eisenmenger, L., Field, A., Davidson, R., Johnson, S., Asthana, S., Chin, N., Prabhakaran, V., Bendlin, B., et al., 2023. Incidental findings from 16,400 brain mri examinations of research volunteers. *American Journal of Neuroradiology* 44, 417–423.
- Schlegl, T., Seeböck, P., Waldstein, S.M., Langs, G., Schmidt-Erfurth, U., 2019. f-anogan: Fast unsupervised anomaly detection with generative adversarial networks. *Medical image analysis* 54, 30–44.
- Stollenga, M.F., Byeon, W., Liwicki, M., Schmidhuber, J., 2015. Parallel multi-dimensional lstm, with application to fast biomedical volumetric image segmentation. *Advances in neural information processing systems* 28.
- Wolleb, J., Bieder, F., Sandkühler, R., Cattin, P.C., 2022. Diffusion models for medical anomaly detection, in: International Conference on Medical image computing and computer-assisted intervention, Springer. pp. 35–45.
- Wu, J., Fu, R., Fang, H., Zhang, Y., Yang, Y., Xiong, H., Liu, H., Xu, Y., 2024. Medsegdiff: Medical image segmentation with diffusion probabilistic model, in: Medical Imaging with Deep Learning, PMLR. pp. 1623–1639.
- Xu, W., Moffat, M., Seale, T., Liang, Z., Wagner, F., Whitehouse, D., Menon, D., Newcombe, V., Voets, N., Banerjee, A., et al., 2024. Feasibility and benefits of joint learning from mri databases with different brain diseases and modalities for segmentation. *arXiv preprint arXiv:2405.18511* .
- Zheng, J.Q., Mo, Y., Sun, Y., Li, J., Wu, F., Wang, Z., Vincent, T., Papież, B.W., 2024. Deformation-recovery diffusion model (drdm): Instance deformation for image manipulation and synthesis. *arXiv preprint arXiv:2407.07295* .
- Zimmerer, D., Isensee, F., Petersen, J., Kohl, S., Maier-Hein, K., 2019. Unsupervised anomaly localization using variational auto-encoders, in: Medical Image Computing and Computer Assisted Intervention–MICCAI 2019: 22nd International Conference, Shenzhen, China, October 13–17, 2019, Proceedings, Part IV 22, Springer. pp. 289–297.